Soil Dynamics and Earthquake Engineering 31 (2011) 729–736

Contents lists available at ScienceDirect

Soil Dynamics and Earthquake Engineering

journal homepage: www.elsevier.com/locate/soildyn

SH-wave diffraction by a semi-circular hill revisited: A null-field boundary integral equation method using degenerate kernels

Jeng-Tzong Chen [a,b,*], Jia-Wei Lee [a], Chine-Feng Wu [a], I-Lin Chen [c]

[a] *Department of Harbor and River Engineering, National Taiwan Ocean University, Keelung, Taiwan*
[b] *Department of Mechanical and Mechatronic Engineering, National Taiwan Ocean University, Keelung, Taiwan*
[c] *Department of Naval Architecture, National Kaohsiung Marine University, Kaohsiung, Taiwan*

ARTICLE INFO

Article history:
Received 8 September 2010
Received in revised form
28 November 2010
Accepted 1 December 2010
Available online 26 January 2011

Keywords:
SH-wave
Diffraction
Semi-circular hill
Null-field BIEM
Degenerate kernel

ABSTRACT

Following the success of seismic analysis of a canyon [1], the problem of SH-wave diffraction by a semi-circular hill is revisited using the null-field boundary integral equation method (BIEM). To fully utilize the analytical property in the null-field boundary integral equation approach in conjunction with degenerate kernels for solving the semi-circular hill scattering problem, the problem is decomposed into two regions to produce circular boundaries using the technique of taking free body. One is the half-plane problem containing a semi-circular boundary. This semi-infinite problem is imbedded in an infinite plane with an artificial full circular boundary such that degenerate kernel can be fully applied. The other is an interior problem bounded by a circular boundary. The degenerate kernel in the polar coordinates for two subdomains is utilized for the closed-form fundamental solution. The semi-analytical formulation along with matching boundary conditions yields six constraint equations. Instead of finding admissible wave expansion bases, our null-field BIEM approach in conjunction with degenerate kernels have five features over the conventional BIEM/BEM: (1) free from calculating principal values, (2) exponential convergence, (3) elimination of boundary-layer effect, (4) meshless and (5) well-posed system. All the numerical results are comparing well with the available results in the literature. It is interesting to find that a focusing phenomenon is also observed in this study.

1. Introduction

Taiwan is located in the Pacific Ring of Fire, which is an area with a large number of earthquakes and volcanic eruptions. It results in significant displacement amplitude on the canyon, hill, and ground surface due to scattering and diffraction of seismic waves. Studying the vibrational response of the soil due to earthquakes is an important issue in this area. Based on assumptions of linear elastic, isotropic and homogenous medium for the soil, problems of SH-wave diffraction can be formulated to the two-dimensional Helmholtz equation.

Regarding problems of SH-wave diffraction and scattering by the alluvial valley and canyon, Trifunac derived analytical solutions for semi-circular cases with alluvial and without alluvial in 1971 [2] and 1973 [3], respectively. Later, Yuan and Liao [4] employed the approach of wave function expansion to deal with problems of SH-waves scattered by a cylindrical canyon of circular-arc cross-section. For the multi-layers problems, Vogt et al. [5] have employed the indirect-boundary element method (BEM) to solve the canyon problem of arbitrary shape in a layered half-space. The reflection waves caused by a hill are more complex than by a canyon from the point of wave physics. Mathematically speaking, hill scattering is more difficult than the canyon case due to not only its convex geometry but also its solution space. It means that the closed-form or analytical solution is not easy to derive. Therefore, numerical methods are required.

Numerical methods were used to solve this kind of problems including wave function expansion method [6–8], BIEM/BEM [1], hybrid method [9] and spectral-element method (SEM) [10]. For the boundary element methods (BEM), direct [11,12] and indirect formulations [13] have been employed. Regarding the fundamental solution, Kawase [14] used the discrete wave number Green's function in BEM. For the conventional BEM, the closed-form fundamental solutions is utilized. Chen and his coworkers employed the degenerate kernel for the fundamental solution and proposed the null-field integral equation approach. To consider the complex shape of canyon or hill, hybrid method and SEM are flexible to solve this problem. The main point to care about for the wave function expansion method is the selection of completeness of the wave function base. As quoted by Tsaur and Chang [6] "Unfortunately, their series solution for such a problem is in error due to unsuitable connection between the domain decomposition and the expression of corresponding wavefield."; this

* Corresponding author at: Department of Harbor and River Engineering, National Taiwan Ocean University, Keelung, Taiwan. Tel.: +886 2 24622192x6177; fax: +886 2 24632375.
E-mail address: jtchen@mail.ntou.edu.tw (J.-T. Chen).

0267-7261/$ - see front matter © 2010 Elsevier Ltd. All rights reserved.
doi:10.1016/j.soildyn.2010.12.001

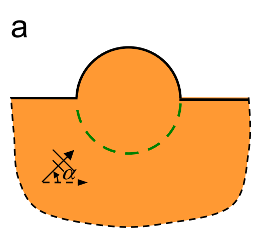

Fig. 1. Decomposition of scattering problem with semi-circular topography. (a) Seismic analysis for a hill scattering and (b) harbor resonance and electromagnetics.

pointed out that finding admissible bases is important. This is the reason why Lee et al. [15] improved the analytical wave series solution of Yuan and Men's [7] and Yuan and Liao's [8] papers to take care of the stress singularity on the rim of the hill. A convenient criterion of completeness was mentioned by Sánchez-Sesma et al. [16]. The expansion can converge uniformly if Rayleigh hypothesis is satisfied.

In 2008, Chen et al. [1] employed the null-field BIEM to solve SH-wave diffraction problems by multiple semi-circular alluvial valleys. Due to the circular geometry, Chen and his coworkers naturally employed the null-field BIEM in conjunction with degenerate kernels and Fourier series. Therefore, their proposed approach is a semi-analytical approach. The expansion of closed-form fundamental solution is also one kind of addition theorem that has been widely used in the approach of wave function expansion. Besides, five features over the conventional BIEM/BEM: (1) free from calculating principal values, (2) exponential convergence, (3) elimination of boundary-layer effect, (4) meshless and (5) well-posed system, were demonstrated. A large amount of work to demonstrate the five advantages have been done by Chen and his coworkers for Laplace [17], Helmholtz [18], biharmonic [19] and bittelmholtz [20] problems.

No matter what approach is used, a benchmark example to demonstrate the validity of numerical approaches is required. For hill scattering cases, three popular examples, semi-circular hill [7], Gaussian hill [21] and half-sine hill [22], have been widely used. For simplicity, a semi-circular hill is our focus by testing our formulation. To deal with this problem, the idea of domain decomposition was used in earthquake, ocean and electrical engineering. It is interesting to find that earthquake engineers always cut the circular arc to have a circular region as the second domain [7], as shown in Fig. 1(a). In harbor resonance [23] and electromagnetics [24], a straight line is introduced to separate into two regions, as shown in Fig. 1b.

Focusing effect in optics, acoustics and electromagnetics has been noticed, but only a little in elastic wave was recorded. Tsaur and Chang [6] employed the wave function expansion approach to find the focusing behavior for the shallow circular arc hill in both time and frequency domains. The maximum response may occur beneath the hill boundary, which may cause failure for underground structures. In this paper, we also have an interest to search for the possible focusing in the semi-circular hill.

Accordingly, we aim to extend the approach to deal with SH-wave diffraction problems by a semi-circular hill. Instead of finding admissible wave function expansion bases, we construct six constraint equations from the null-field BIE formulations and matching boundary conditions. Numerical results will be compared with the available results in the literature.

2. Problem statement

A scattering problem subject to a SH wave impinging on a semi-circular hill is shown in Fig. 2(a). The material property of the soil is assumed to be linear elastic, isotropic and homogenous. Therefore, the governing equation of the anti-plane motion is the two-dimensional Helmholtz equation as follows:

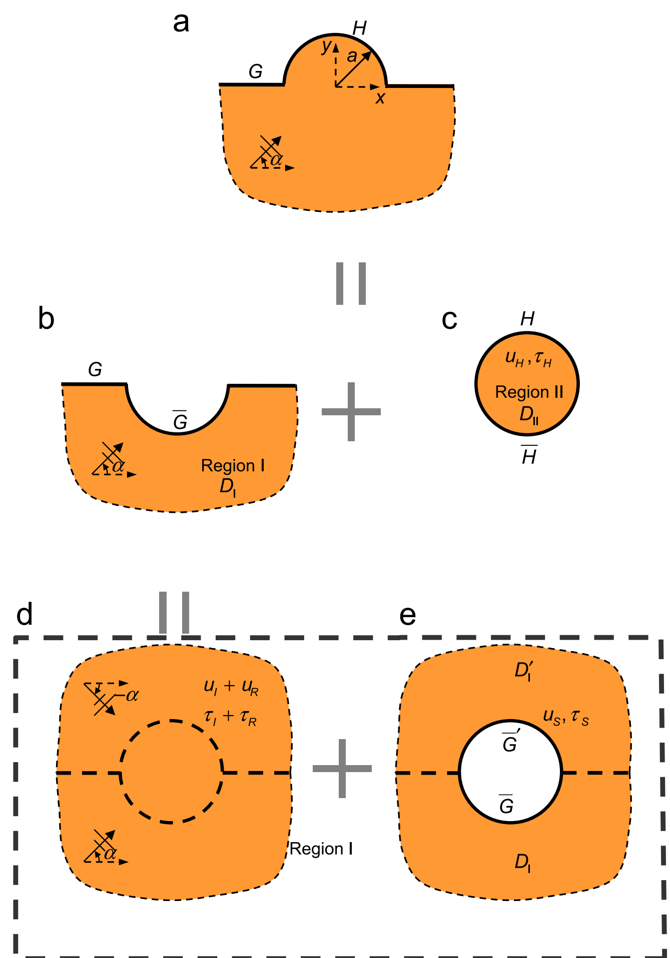

Fig. 2. Decomposition of the semi-circular hill scattering problem. (a) Original problem, (b) a half-plane subject to traction free B.C. along the horizontal ground surface, (c) a circular region, (d) an infinite plane and (e) an infinite plane containing a circular hole.

$$(\nabla^2 + k^2)u(\mathbf{x}) = 0, \quad \mathbf{x} \in D, \tag{1}$$

where ∇^2 is the Laplacian operator, k is the shear wave number, $u(\mathbf{x})$ is the anti-plane displacement of the semi-circular hill, $\mathbf{x}$ is the field point and D is the domain of interest. The two components of the field point $\mathbf{x}$ for the Cartesian and polar coordinates are (x,y) and (ρ,ϕ), respectively. The boundary condition is the traction-free boundary condition as shown below:

$$\tau(\mathbf{x}) = \mu t(\mathbf{x}) = \mu \frac{\partial u(\mathbf{x})}{\partial n_{\mathbf{x}}} = 0, \quad \mathbf{x} \in B, \tag{2}$$

where $\tau(\mathbf{x})$ is the traction along the boundary, $t(\mathbf{x})$ is the normal derivative of $u(\mathbf{x})$, μ is the shear modulus, $n_{\mathbf{x}}$ denotes the unit outward normal vector at the field point and B is the boundary. Besides, the traction free boundary condition can be represented by using the polar coordinates as shown below:

$$\tau(\rho,\phi) = \mu \frac{\partial u(\rho,\phi)}{\partial \rho} = 0, \quad \rho = a, \quad 0 \le \phi \le \pi, \tag{3}$$

$$\tau(\rho,\phi) = \mu \frac{1}{\rho}\cos(\phi)\frac{\partial u(\rho,\phi)}{\partial \phi} = 0, \quad \rho > a, \quad \phi = 0 \text{ or } \pi, \tag{4}$$

where a is the radius of the semi-circular hill.

The incident plane SH wave is expressed as

$$u_I(\mathbf{x}) = A_0 e^{ik(x\cos(\alpha)+y\sin(\alpha))}, \tag{5}$$

where A_0 is the amplitude of the SH wave and α is the incident angle.

3. Dual boundary integral formulations and degenerate kernels

Introducing the degenerate kernels, the collocation point can be located on the real boundary without the need of calculating the principal value. Therefore, the representations of conventional integral equations including the boundary point can be written as

$$2\pi u(\mathbf{x}) = \int_B T(\mathbf{s},\mathbf{x})u(\mathbf{s})dB(\mathbf{s}) - \int_B U(\mathbf{s},\mathbf{x})t(\mathbf{s})dB(\mathbf{s}), \quad \mathbf{x} \in D \cup B, \tag{6}$$

$$2\pi t(\mathbf{x}) = \int_B M(\mathbf{s},\mathbf{x})u(\mathbf{s})dB(\mathbf{s}) - \int_B L(\mathbf{s},\mathbf{x})t(\mathbf{s})dB(\mathbf{s}), \quad \mathbf{x} \in D \cup B, \tag{7}$$

and

$$0 = \int_B T(\mathbf{s},\mathbf{x})u(\mathbf{s})dB(\mathbf{s}) - \int_B U(\mathbf{s},\mathbf{x})t(\mathbf{s})dB(\mathbf{s}), \quad \mathbf{x} \in D^c \cup B, \tag{8}$$

$$0 = \int_B M(\mathbf{s},\mathbf{x})u(\mathbf{s})dB(\mathbf{s}) - \int_B L(\mathbf{s},\mathbf{x})t(\mathbf{s})dB(\mathbf{s}), \quad \mathbf{x} \in D^c \cup B, \tag{9}$$

where $\mathbf{s}$ is the source point, D^c is the complementary domain and the kernel function $U(\mathbf{s},\mathbf{x})$ is the fundamental solution that satisfies

$$(\nabla^2 + k^2)U(\mathbf{s},\mathbf{x}) = 2\pi\delta(\mathbf{x}-\mathbf{s}), \tag{10}$$

in which $\delta(\mathbf{x}-\mathbf{s})$ denotes the Dirac-delta function. It is noted that the four kernels in Eqs. (6)–(9) should be chosen for the corresponding degenerate kernels. The other kernel functions, $T(\mathbf{s},\mathbf{x})$, $L(\mathbf{s},\mathbf{x})$ and $M(\mathbf{s},\mathbf{x})$, are defined by

$$T(\mathbf{s},\mathbf{x}) = \frac{\partial U(\mathbf{s},\mathbf{x})}{\partial n_{\mathbf{s}}}, \tag{11}$$

$$L(\mathbf{s},\mathbf{x}) = \frac{\partial U(\mathbf{s},\mathbf{x})}{\partial n_{\mathbf{x}}}, \tag{12}$$

$$M(\mathbf{s},\mathbf{x}) = \frac{\partial^2 U(\mathbf{s},\mathbf{x})}{\partial n_{\mathbf{s}}\partial n_{\mathbf{x}}}, \tag{13}$$

where $n_{\mathbf{s}}$ denotes the unit outward normal vector at the source point. It is noted that Eqs. (6)–(9) can contain the boundary point ($\mathbf{x} \to B$) since the kernel functions (U, T, L and M) are expressed in terms of various degenerate kernels that will be elaborated on later in Eqs. (19)–(22).

The closed-form fundamental solution as previously mentioned is

$$U(\mathbf{s},\mathbf{x}) = -\frac{i\pi H_0^{(1)}(kr)}{2}, \tag{14}$$

where $r \equiv |\mathbf{s}-\mathbf{x}|$ is the distance between the source point and the field point and $H_0^{(1)}$ is the zeroth-order Hankel function of the first kind. Based on the property of separation variables in the polar coordinates, the closed-form fundamental solution $U(\mathbf{s},\mathbf{x})$ of Eq. (14), other kernel functions, $T(\mathbf{s},\mathbf{x})$ $L(\mathbf{s},\mathbf{x})$, and $M(\mathbf{s},\mathbf{x})$, can be expressed as

$$U(\mathbf{s},\mathbf{x}) = \begin{cases} U^E(\mathbf{s},\mathbf{x}) = \lim_{N\to\infty} U_N^E(\mathbf{s},\mathbf{x}), & \rho \ge R, \\ U^I(\mathbf{s},\mathbf{x}) = \lim_{N\to\infty} U_N^I(\mathbf{s},\mathbf{x}), & \rho < R, \end{cases} \tag{15}$$

$$T(\mathbf{s},\mathbf{x}) = \begin{cases} T^E(\mathbf{s},\mathbf{x}) = \lim_{N\to\infty} T_N^E(\mathbf{s},\mathbf{x}), & \rho > R, \\ T^I(\mathbf{s},\mathbf{x}) = \lim_{N\to\infty} T_N^I(\mathbf{s},\mathbf{x}), & \rho < R, \end{cases} \tag{16}$$

$$L(\mathbf{s},\mathbf{x}) = \begin{cases} L^E(\mathbf{s},\mathbf{x}) = \lim_{N\to\infty} L_N^E(\mathbf{s},\mathbf{x}), & \rho > R, \\ L^I(\mathbf{s},\mathbf{x}) = \lim_{N\to\infty} L_N^I(\mathbf{s},\mathbf{x}), & \rho < R, \end{cases} \tag{17}$$

$$M(\mathbf{s},\mathbf{x}) = \begin{cases} M^E(\mathbf{s},\mathbf{x}) = \lim_{N\to\infty} M_N^E(\mathbf{s},\mathbf{x}), & \rho \ge R, \\ M^I(\mathbf{s},\mathbf{x}) = \lim_{N\to\infty} M_N^I(\mathbf{s},\mathbf{x}), & \rho < R, \end{cases} \tag{18}$$

where $U_N^E(\mathbf{s},\mathbf{x})$, $U_N^I(\mathbf{s},\mathbf{x})$, $T_N^E(\mathbf{s},\mathbf{x})$, $T_N^I(\mathbf{s},\mathbf{x})$, $L_N^E(\mathbf{s},\mathbf{x})$, $L_N^I(\mathbf{s},\mathbf{x})$, $M_N^E(\mathbf{s},\mathbf{x})$ and $M_N^I(\mathbf{s},\mathbf{x})$ are degenerate kernels as shown below:

$$\begin{cases} U_N^E(\mathbf{s},\mathbf{x}) = \frac{-\pi i}{2}\sum_{m=0}^{N} \varepsilon_m J_m(kR)H_m^{(1)}(k\rho)\cos(m(\theta-\phi)), & \rho \ge R, \\ U_N^I(\mathbf{s},\mathbf{x}) = \frac{-\pi i}{2}\sum_{m=0}^{N} \varepsilon_m J_m(k\rho)H_m^{(1)}(kR)\cos(m(\theta-\phi)), & \rho < R, \end{cases} \tag{19}$$

$$\begin{cases} T_N^E(\mathbf{s},\mathbf{x}) = \frac{-\pi ki}{2}\sum_{m=0}^{N} \varepsilon_m J'_m(kR)H_m^{(1)}(k\rho)\cos(m(\theta-\phi)), & \rho > R, \\ T_N^I(\mathbf{s},\mathbf{x}) = \frac{-\pi ki}{2}\sum_{m=0}^{N} \varepsilon_m J_m(k\rho)H'^{(1)}_m(kR)\cos(m(\theta-\phi)), & \rho < R, \end{cases} \tag{20}$$

$$\begin{cases} L_N^E(\mathbf{s},\mathbf{x}) = \frac{-\pi ki}{2}\sum_{m=0}^{N} \varepsilon_m J_m(kR)H'^{(1)}_m(k\rho)\cos(m(\theta-\phi)), & \rho > R, \\ L_N^I(\mathbf{s},\mathbf{x}) = \frac{-\pi ki}{2}\sum_{m=0}^{N} \varepsilon_m J'_m(k\rho)H_m^{(1)}(kR)\cos(m(\theta-\phi)), & \rho < R, \end{cases} \tag{21}$$

$$\begin{cases} M_N^E(\mathbf{s},\mathbf{x}) = \frac{-\pi k^2 i}{2}\sum_{m=0}^{N} \varepsilon_m J'_m(kR)H'^{(1)}_m(k\rho)\cos(m(\theta-\phi)), & \rho \ge R, \\ M_N^I(\mathbf{s},\mathbf{x}) = \frac{-\pi k^2 i}{2}\sum_{m=0}^{N} \varepsilon_m J'_m(k\rho)H'^{(1)}_m(kR)\cos(m(\theta-\phi)), & \rho < R, \end{cases} \tag{22}$$

in which (R, θ) are the polar coordinates of the source point $\mathbf{s}$, J_m is the mth-order Bessel function of the first kind and ε_m is the Neumann factor,

$$\varepsilon_m = \begin{cases} 1, & m = 0, \\ 2, & m = 1, 2, \ldots, \infty. \end{cases} \tag{23}$$

4. Decomposition of the problem and six constraints

4.1. Decomposition of the problem

In order to fully utilize the semi-analytical property of the null-field BIEM for solving boundary value problems containing circular boundaries, the original problem of a semi-circular hill is divided into two regions as shown in Fig. 2(a), where G and H denote the horizontal ground surface and semi-circular hill border, respectively. A half-plane region (Region I) is shown in Fig. 2(b) and the other is an enclosed region bounded by the circular boundary (Region II) as shown in Fig. 2(c). In Fig. 2(b), a half-plane with an artificial boundary ($\overline{G}$) can be imbedded to an infinite. Then, it can be decomposed into an infinite plane with incident and reflective waves and an infinite plane containing a circular hole that satisfies the specified boundary condition as shown in Fig. 2(d) and (e), respectively.

4.2. Expansion of boundary density

To fully utilize the geometry of circular boundary, the boundary displacement $u(\mathbf{s})$ and boundary normal stress $\tau(\mathbf{s})$ along the circular boundary can be approximated by employing the Fourier series. Therefore, we obtain

$$u_S(\mathbf{s}) = u_S(\theta) = a_0^S + \sum_{n=1}^{\infty}(a_n^S \cos n\theta + b_n^S \sin n\theta), \tag{24}$$

$$\tau_S(\mathbf{s}) = \mu t_S(\mathbf{s}) = \mu t_S(\theta) = \mu\left(p_0^S + \sum_{n=1}^{\infty}(p_n^S \cos n\theta + q_n^S \sin n\theta)\right), \tag{25}$$

$$u_H(\mathbf{s}) = u_H(\theta) = a_0^H + \sum_{n=1}^{\infty}(a_n^H \cos n\theta + b_n^H \sin n\theta), \tag{26}$$

$$\tau_H(\mathbf{s}) = \mu t_H(\mathbf{s}) = \mu t_H(\theta) = \mu\left(p_0^H + \sum_{n=1}^{\infty}(p_n^H \cos n\theta + q_n^H \sin n\theta)\right), \tag{27}$$

where a_0^S, a_n^S, b_n^S, p_0^S, p_n^S, q_n^S a_0^H, a_n^H, b_n^H, p_0^H, p_n^H and q_n^H are the Fourier coefficients; the superscripts "S" and "H" denote the regions I in Fig. 2(e) and II in Fig. 2(c), respectively. In the real computation, only the finite $2M+1$ terms are truncated in the summation of Eqs. (24)–(27).

4.3. Formulations for each region and matching of boundary conditions

To formulate the original problem after decomposition, six equations are obtained from BIEs and matching of BCs.

4.3.1. Exterior problem using the null-field BIEM

For the exterior problem containing a circular hole subject to the specified boundary condition as shown in Fig. 2(e) using the null-field BIEM for the boundary point in Eq. (8), we have

$$\int_{\overline{G}\cup\overline{G}'}[T^I(\mathbf{s},\mathbf{x})u_S(\mathbf{s}) - U^I(\mathbf{s},\mathbf{x})t_S(\mathbf{s})]dB(\mathbf{s}) = 0, \quad \mathbf{x}\in\overline{G}\cup\overline{G}' \tag{28}$$

along boundaries $\overline{G}\cup\overline{G}'$.

4.3.2. Interior problem using the null-field BIEM

For the null-field BIEM of the circular domain in Fig. 2(c), we have the null-field BIE for the boundary point of region II:

$$\int_{H\cup\overline{H}}[T^E(\mathbf{s},\mathbf{x})u_H(\mathbf{s}) - U^E(\mathbf{s},\mathbf{x})t_H(\mathbf{s})]dB(\mathbf{s}) = 0, \quad \mathbf{x}\in H\cup\overline{H} \tag{29}$$

along boundaries $H\cup\overline{H}$

4.3.3. Continuity condition and equilibrium condition on the artificial interface

For the continuity condition on the artificial interface, we have

$$u_I(\phi) + u_R(\phi) + u_S(\phi) = u_H(\phi), \quad \pi \le \phi \le 2\pi, \tag{30}$$

$$-(\tau_I(\phi) + \tau_R(\phi) + \tau_S(\phi)) = \tau_H(\phi), \quad \pi \le \phi \le 2\pi, \tag{31}$$

for the displacement and equilibrium condition of stress, respectively.

4.3.4. Boundary condition on the hill border

The hill border boundary (H) is subject to the boundary condition of traction free (Neumann type) in Eq. (3) as shown below:

$$\tau_H(\phi) = 0, \quad 0 \le \phi \le \pi. \tag{32}$$

4.3.5. Boundary condition on the horizontal ground surface

The half-plane with a horizontal ground surface boundary is also subject to the boundary condition of traction free in Eq. (4) as shown below:

$$\mu\frac{\partial u_S(\mathbf{x})}{\partial y} = \mu\int_{\overline{G}\cup\overline{G}'}\left[\frac{\partial T^E(\mathbf{s},\mathbf{x})}{\partial y}u_S(\mathbf{s}) - \frac{\partial U^E(\mathbf{s},\mathbf{x})}{\partial y}t_S(\mathbf{s})\right]dB(\mathbf{s}) = 0, \quad \mathbf{x}\in G, \tag{33}$$

where $\partial U^E(\mathbf{s},\mathbf{x})/\partial y$ and $\partial T^E(\mathbf{s},\mathbf{x})/\partial y$ are shown below:

$$\frac{\partial U^E(\mathbf{s},\mathbf{x})}{\partial y} = \sin(\phi)\frac{\partial U^E(\mathbf{s},\mathbf{x})}{\partial\rho} + \frac{1}{\rho}\cos(\phi)\frac{\partial U^E(\mathbf{s},\mathbf{x})}{\partial\phi}, \tag{34}$$

$$\frac{\partial T^E(\mathbf{s},\mathbf{x})}{\partial y} = \sin(\phi)\frac{\partial T^E(\mathbf{s},\mathbf{x})}{\partial\rho} + \frac{1}{\rho}\cos(\phi)\frac{\partial T^E(\mathbf{s},\mathbf{x})}{\partial\phi}, \tag{35}$$

in which $\partial U^E(\mathbf{s},\mathbf{x})/\partial\rho$, $\partial U^E(\mathbf{s},\mathbf{x})/\partial\phi$, $\partial T^E(\mathbf{s},\mathbf{x})/\partial\rho$ and $\partial T^E(\mathbf{s},\mathbf{x})/\partial\phi$ can be found in the Appendix.

5. Discretization to a linear algebraic equation

5.1. Exterior and interior problems using the null-field BIEM

In order to calculate the Fourier coefficients, $2M+1$ boundary nodes for the circular boundary are needed, Eqs. (28) and (29) are discretized to

$$[\mathbf{T}^I]_{(2M+1)\times(2M+1)}\{\mathbf{u}^S\}_{(2M+1)\times 1} - [\mathbf{U}^I]_{(2M+1)\times(2M+1)}\{\mathbf{t}^S\}_{(2M+1)\times 1} = \{\mathbf{0}\}_{(2M+1)\times 1}, \tag{36}$$

$$[\mathbf{T}^E]_{(2M+1)\times(2M+1)}\{\mathbf{u}^H\}_{(2M+1)\times 1} - [\mathbf{U}^E]_{(2M+1)\times(2M+1)}\{\mathbf{t}^H\}_{(2M+1)\times 1} = \{\mathbf{0}\}_{(2M+1)\times 1}, \tag{37}$$

where $[\mathbf{U}^I]$, $[\mathbf{T}^I]$, $[\mathbf{U}^E]$ and $[\mathbf{T}^E]$ are the influence matrices with a dimension of $2M+1$ by $2M+1$; $\{\mathbf{u}^S\}$, $\{\mathbf{t}^S\}$, $\{\mathbf{u}^H\}$ and $\{\mathbf{t}^H\}$ denote the vectors of $u_S(\mathbf{s})$, $t_S(\mathbf{s})$, $u_H(\mathbf{s})$ and $t_S(\mathbf{s})$ for the generalized coordinates of Fourier coefficients with a dimension of $2M+1$ by 1 as shown below:

$$\{\mathbf{u}^S\} = \left\langle a_0^S \quad a_1^S \quad a_2^S \quad \cdots \quad a_M^S \quad b_1^S \quad b_2^S \quad \cdots \quad b_M^S \right\rangle^T, \tag{38}$$

$$\{\mathbf{t}^S\} = \left\langle p_0^S \quad p_1^S \quad p_2^S \quad \cdots \quad p_M^S \quad q_1^S \quad q_2^S \quad \cdots \quad q_M^S \right\rangle^T, \tag{39}$$

$$\{\mathbf{u}^H\} = \left\langle a_0^H \quad a_1^H \quad a_2^H \quad \cdots \quad a_M^H \quad b_1^H \quad b_2^H \quad \cdots \quad b_M^H \right\rangle^T, \tag{40}$$

$$\{\mathbf{t}^H\} = \left\langle p_0^H \quad p_1^H \quad p_2^H \quad \cdots \quad p_M^H \quad q_1^H \quad q_2^H \quad \cdots \quad q_M^H \right\rangle^T. \tag{41}$$

After uniformly collocating the points along the circular boundary, the influence matrices can be written as

$$[\mathbf{U}] = \begin{bmatrix} U^{0c}(\phi_1) & U^{1c}(\phi_1) & \cdots & U^{Mc}(\phi_1) & U^{1s}(\phi_1) & \cdots & U^{Ms}(\phi_1) \\ U^{0c}(\phi_2) & U^{1c}(\phi_2) & \cdots & U^{Mc}(\phi_2) & U^{1s}(\phi_2) & \cdots & U^{Ms}(\phi_2) \\ U^{0c}(\phi_3) & U^{1c}(\phi_3) & \cdots & U^{Mc}(\phi_3) & U^{1s}(\phi_3) & \cdots & U^{Ms}(\phi_3) \\ \vdots & \vdots & \ddots & \vdots & \vdots & \ddots & \vdots \\ U^{0c}(\phi_{2M}) & U^{1c}(\phi_{2M}) & \cdots & U^{Mc}(\phi_{2M}) & U^{1s}(\phi_{2M}) & \cdots & U^{Ms}(\phi_{2M}) \\ U^{0c}(\phi_{2M+1}) & U^{1c}(\phi_{2M+1}) & \cdots & U^{Mc}(\phi_{2M+1}) & U^{1s}(\phi_{2M+1}) & \cdots & U^{Ms}(\phi_{2M+1}) \end{bmatrix}, \tag{42}$$

$$[\mathbf{T}] = \begin{bmatrix} T^{0c}(\phi_1) & T^{1c}(\phi_1) & \cdots & T^{Mc}(\phi_1) & T^{1s}(\phi_1) & \cdots & T^{Ms}(\phi_1) \\ T^{0c}(\phi_2) & T^{1c}(\phi_2) & \cdots & T^{Mc}(\phi_2) & T^{1s}(\phi_2) & \cdots & T^{Ms}(\phi_2) \\ T^{0c}(\phi_3) & T^{1c}(\phi_3) & \cdots & T^{Mc}(\phi_3) & T^{1s}(\phi_3) & \cdots & T^{Ms}(\phi_3) \\ \vdots & \vdots & \ddots & \vdots & \vdots & \ddots & \vdots \\ T^{0c}(\phi_{2M}) & T^{1c}(\phi_{2M}) & \cdots & T^{Mc}(\phi_{2M}) & T^{1s}(\phi_{2M}) & \cdots & T^{Ms}(\phi_{2M}) \\ T^{0c}(\phi_{2M+1}) & T^{1c}(\phi_{2M+1}) & \cdots & T^{Mc}(\phi_{2M+1}) & T^{1s}(\phi_{2M+1}) & \cdots & T^{Ms}(\phi_{2M+1}) \end{bmatrix}. \tag{43}$$

Although both matrices in Eqs. (42) and (43) are not sparse, it is found that the higher-order harmonics is considered, and the smaller influence coefficients in numerical experiments are obtained. It is noted that the superscript "0s" in Eqs. (42) and (43) disappears since $\sin(0\theta)$. The elements of $[\mathbf{U}]$ and $[\mathbf{T}]$ are defined, respectively, as

$$U^{nc}(\phi_L)=\int_0^{2\pi} U(\mathbf{s},\mathbf{x}_L)\cos(n\theta)ad\theta, \tag{44}$$

$$U^{\overline{n}s}(\phi_L)=\int_0^{2\pi} U(\mathbf{s},\mathbf{x}_L)\sin(\overline{n}\theta)ad\theta, \tag{45}$$

$$T^{nc}(\phi_L)=\int_0^{2\pi} T(\mathbf{s},\mathbf{x}_L)\cos(n\theta)ad\theta, \tag{46}$$

$$T^{\overline{n}s}(\phi_L)=\int_0^{2\pi} T(\mathbf{s},\mathbf{x}_L)\sin(\overline{n}\theta)ad\theta, \tag{47}$$

where $n=0,1,2,\ldots, M$, $\overline{n}=1,2,\ldots, M$ and $L=1,2,\ldots, 2M+1$, and ϕ_L is the polar angle of the collocation point $\mathbf{x}_L$.

$$\left[\mathbf{U}_y^E\right]=\begin{bmatrix} U_y^{0c}(\phi_1) & U_y^{1c}(\phi_1) & \cdots & U_y^{Mc}(\phi_1) & U_y^{1s}(\phi_1) & \cdots & U_y^{Ms}(\phi_1) \\ U_y^{0c}(\phi_2) & U_y^{1c}(\phi_2) & \cdots & U_y^{Mc}(\phi_2) & U_y^{1s}(\phi_2) & \cdots & U_y^{Ms}(\phi_2) \\ U_y^{0c}(\phi_3) & U_y^{1c}(\phi_3) & \cdots & U_y^{Mc}(\phi_3) & U_y^{1s}(\phi_3) & \cdots & U_y^{Ms}(\phi_3) \\ \vdots & \vdots & \ddots & \vdots & \vdots & \ddots & \vdots \\ U_y^{0c}(\phi_{N_{hgs}-1}) & U_y^{1c}(\phi_{N_{hgs}-1}) & \cdots & U_y^{Mc}(\phi_{N_{hgs}-1}) & U_y^{1s}(\phi_{N_{hgs}-1}) & \cdots & U_y^{Ms}(\phi_{N_{hgs}-1}) \\ U_y^{0c}(\phi_{N_{hgs}}) & U_y^{1c}(\phi_{N_{hgs}}) & \cdots & U_y^{Mc}(\phi_{N_{hgs}}) & U_y^{1s}(\phi_{N_{hgs}}) & \cdots & U_y^{Ms}(\phi_{N_{hgs}}) \end{bmatrix}, \tag{56}$$

$$[\mathbf{T}_\mathbf{y}^E]=\begin{bmatrix} T_y^{0c}(\phi_1) & T_y^{1c}(\phi_1) & \cdots & T_y^{Mc}(\phi_1) & T_y^{1s}(\phi_1) & \cdots & T_y^{Ms}(\phi_1) \\ T_y^{0c}(\phi_2) & T_y^{1c}(\phi_2) & \cdots & T_y^{Mc}(\phi_2) & T_y^{1s}(\phi_2) & \cdots & T_y^{Ms}(\phi_2) \\ T_y^{0c}(\phi_3) & T_y^{1c}(\phi_3) & \cdots & T_y^{Mc}(\phi_3) & T_y^{1s}(\phi_3) & \cdots & T_y^{Ms}(\phi_3) \\ \vdots & \vdots & \ddots & \vdots & \vdots & \ddots & \vdots \\ T_y^{0c}(\phi_{N_{hgs}-1}) & T_y^{1c}(\phi_{N_{hgs}-1}) & \cdots & T_y^{Mc}(\phi_{N_{hgs}-1}) & T_y^{1s}(\phi_{N_{hgs}-1}) & \cdots & T_y^{Ms}(\phi_{N_{hgs}-1}) \\ T_y^{0c}(\phi_{N_{hgs}}) & T_y^{1c}(\phi_{N_{hgs}}) & \cdots & T_y^{Mc}(\phi_{N_{hgs}}) & T_y^{1s}(\phi_{N_{hgs}}) & \cdots & T_y^{Ms}(\phi_{N_{hgs}}) \end{bmatrix}, \tag{57}$$

5.2. Continuity condition on the artificial interface

Matching the interface conditions at the artificial interface ($\overline{G}$ or $\overline{H}$), Eqs. (30) and (31) can be rewritten as

$$u_S(\phi)-u_H(\phi)=-(u_I(\phi)+u_R(\phi)),\quad \pi\le\phi\le 2\pi, \tag{48}$$

$$\tau_S(\phi)+\tau_H(\phi)=-(\tau_I(\phi)+\tau_R(\phi)),\quad \pi\le\phi\le 2\pi, \tag{49}$$

by collocating N_{ai} nodes, and we have

$$[\mathbf{Q}_{ai}]_{N_{ai}\times(2M+1)}\{\mathbf{u}^S\}_{(2M+1)\times 1}-[\mathbf{Q}_{ai}]_{N_{ai}\times(2M+1)}\{\mathbf{u}^H\}_{(2M+1)\times 1}=-\{\mathbf{u}_I+\mathbf{u}_R\}_{N_{ai}\times 1}, \tag{50}$$

$$[\mathbf{Q}_{ai}]_{N_{ai}\times(2M+1)}\{\mathbf{t}^S\}_{(2M+1)\times 1}+[\mathbf{Q}_{ai}]_{N_{ai}\times(2M+1)}\{\mathbf{t}^H\}_{(2M+1)\times 1}=-\{\mathbf{t}_I+\mathbf{t}_R\}_{N_{ai}\times 1}, \tag{51}$$

where N_{ai} is the number of boundary nodes on the artificial interface as shown in Fig. 3 and $[\mathbf{Q}_{ai}]$ is defined by

$$[\mathbf{Q}_{ai}]=\begin{bmatrix} 1 & \cos(1\phi_1) & \cdots & \cos(M\phi_1) & \sin(1\phi_1) & \cdots & \sin(M\phi_1) \\ 1 & \cos(1\phi_2) & \cdots & \cos(M\phi_2) & \sin(1\phi_2) & \cdots & \sin(M\phi_2) \\ \vdots & \vdots & \ddots & \vdots & \vdots & \ddots & \vdots \\ 1 & \cos(1\phi_{N_{ai}-1}) & \cdots & \cos(M\phi_{N_{ai}-1}) & \sin(1\phi_{N_{ai}-1}) & \cdots & \sin(M\phi_{N_{ai}-1}) \\ 1 & \cos(1\phi_{N_{ai}}) & \cdots & \cos(M\phi_{N_{ai}}) & \sin(1\phi_{N_{ai}}) & \cdots & \sin(M\phi_{N_{ai}}) \end{bmatrix}_{N_{ai}\times(2M+1)}. \tag{52}$$

5.3. Boundary condition on the hill border

Distributing N_{hb} collocation points at the hill border of Region II in Eq. (32), we have

$$[\mathbf{Q}_{hb}]_{N_{hb}\times(2M+1)}\{\mathbf{t}^H\}_{(2M+1)\times 1}=-\{\mathbf{0}\}_{N_{hb}\times 1}, \tag{53}$$

where N_{hb} is the number of collocation points on the hill border (H) as shown in Fig. 3 and $[\mathbf{Q}_{hb}]$ is

$$[\mathbf{Q}_{hb}]=\begin{bmatrix} 1 & \cos(1\phi_1) & \cdots & \cos(M\phi_1) & \sin(1\phi_1) & \cdots & \sin(M\phi_1) \\ 1 & \cos(1\phi_2) & \cdots & \cos(M\phi_2) & \sin(1\phi_2) & \cdots & \sin(M\phi_2) \\ \vdots & \vdots & \ddots & \vdots & \vdots & \ddots & \vdots \\ 1 & \cos(1\phi_{N_{hb}-1}) & \cdots & \cos(M\phi_{N_{hb}-1}) & \sin(1\phi_{N_{hb}-1}) & \cdots & \sin(M\phi_{N_{hb}-1}) \\ 1 & \cos(1\phi_{N_{hb}}) & \cdots & \cos(M\phi_{N_{hb}}) & \sin(1\phi_{N_{hb}}) & \cdots & \sin(M\phi_{N_{hb}}) \end{bmatrix}_{N_{hb}\times(2M+1)}. \tag{54}$$

5.4. Boundary condition on the horizontal ground surface

Collocating N_{hgs} nodes to match the traction free boundary conditions along the horizontal ground surface in Eq. (33), we have

$$[\mathbf{T}_\mathbf{y}^E]_{N_{hgs}\times(2M+1)}\{\mathbf{u}^S\}_{(2M+1)\times 1}-[\mathbf{U}_\mathbf{y}^E]_{N_{hgs}\times(2M+1)}\{\mathbf{t}^S\}_{(2M+1)\times 1}=\{\mathbf{0}\}_{N_{hgs}\times 1}, \tag{55}$$

where

where N_{hgs} is the number of collocation points on the horizontal ground surface (G) as shown in Fig. 3.

Assembling the matrices from the six equations, Eqs. (36), (37), (50), (51), (53) and (55), we have

$$\begin{bmatrix} \mathbf{T}^S & -\mathbf{U}^S & 0 & \mathbf{0} \\ \mathbf{0} & \mathbf{0} & \mathbf{T}^H & -\mathbf{U}^H \\ \mathbf{Q}_{ai} & \mathbf{0} & -\mathbf{Q}_{ai} & \mathbf{0} \\ \mathbf{0} & \mathbf{Q}_{ai} & \mathbf{0} & \mathbf{Q}_{ai} \\ \mathbf{0} & \mathbf{0} & \mathbf{0} & \mathbf{Q}_{hb} \\ \mathbf{T}_\mathbf{y}^S & -\mathbf{U}_\mathbf{y}^S & \mathbf{0} & \mathbf{0} \end{bmatrix}_{(8M+4)\times(8M+4)} \begin{Bmatrix} \mathbf{u}^S \\ \mathbf{t}^S \\ \mathbf{u}^H \\ \mathbf{t}^H \end{Bmatrix}_{(8M+4)\times 1} = \begin{Bmatrix} \mathbf{0} \\ \mathbf{0} \\ -\mathbf{u}_I-\mathbf{u}_R \\ -\mathbf{t}_I-\mathbf{t}_R \\ \mathbf{0} \\ \mathbf{0} \end{Bmatrix}_{(8M+4)\times 1}. \tag{58}$$

where $2N_{ai}+N_{hb}+N_{hgs}=4M+2$. According to the linear algebraic equation in Eq. (58), all the Fourier coefficients can be easily obtained.

6. A numerical example

Here, we consider a semi-circular hill subject to a SH wave as shown in Fig. 2(a). The dimensionless frequency η is defined as

$$\eta=\frac{\omega a}{\pi c}=\frac{ka}{\pi}=\frac{2a}{\lambda}, \tag{59}$$

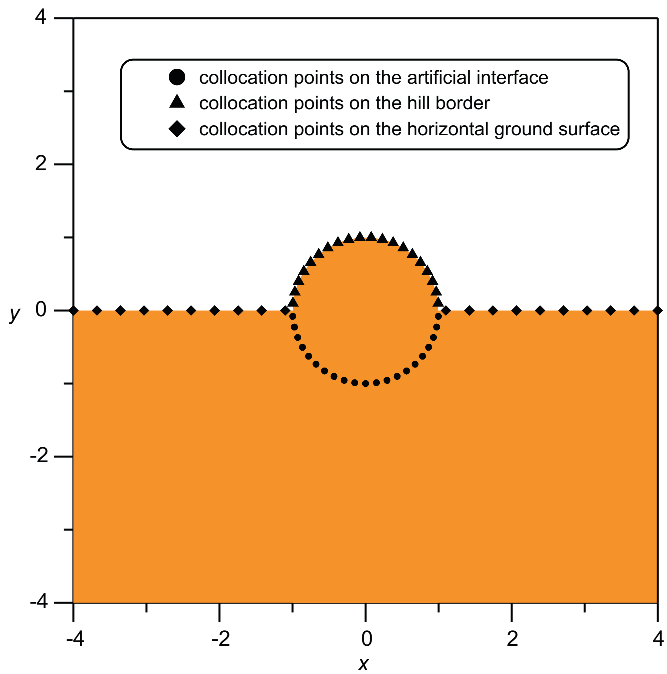

Fig. 3. Distribution of collocation points for the semi-circular hill scattering problem.

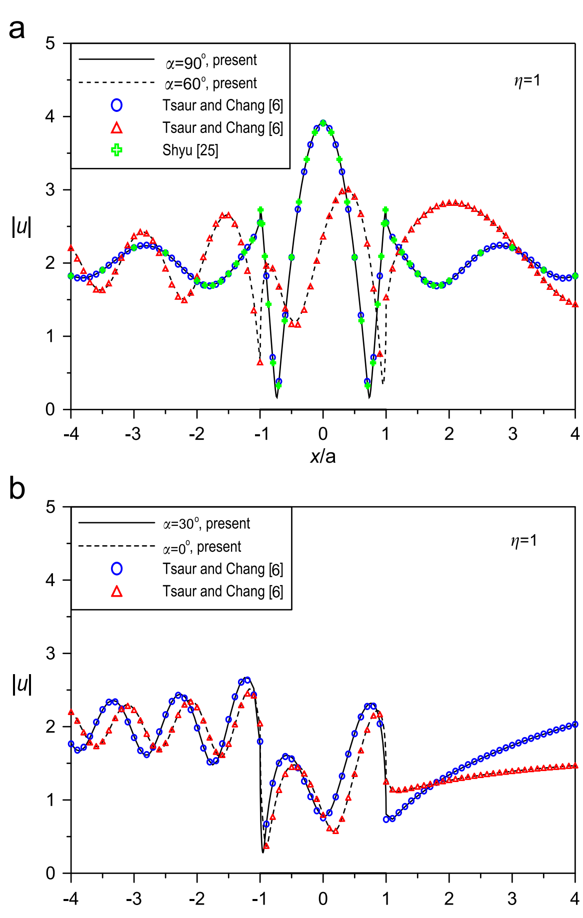

Fig. 4. Surface displacement amplitudes versus x/a for the dimensionless frequency $\eta=1$. (a) $\alpha=90^{\circ}$ and 60° and (b) $\alpha=30^{\circ}$and 0°.

where ω is the angular frequency, c is the velocity of shear wave and λ is the shear wave length. The displacement amplitude is an important index for the earthquake engineering. If the shear modulus is $\mu=1$ and amplitude of incident plane SH-wave is $A_0=1$, the responses at different locations represent amplifications of the incident plane SH-wave wave. The displacement amplitude is defined by

$$|u| = \begin{cases} |u_I+u_R+u_S| = \sqrt{[\mathrm{Re}(u_I+u_R+u_S)]^2+[\mathrm{Im}(u_I+u_R+u_S)]^2}, & \text{for Region I,} \\ |u_H| = \sqrt{[\mathrm{Re}(u_H)]^2+[\mathrm{Im}(u_H)]^2}, & \text{for Region II,} \end{cases} \tag{60}$$

where $\mathrm{Re}(\cdot)$ and $\mathrm{Im}(\cdot)$ are the real and imaginary parts of the displacement, respectively. Fig. 4(a) and (b) show the surface displacement amplitude versus x/a for the dimensionless frequency $\eta=1$, and the corresponding position of the hill border is within the range $x/a=-1.0\sim1.0$ (bold line). Fig. 4(a) and (b) show the displacement amplitude versus x/a for the incident angle of $\alpha=0^{\circ}$, 30°, 60° and 90° and the results of Shyu [25] and Tsaur and Chang [6] are also plotted for comparisons. Fig. 5 shows the surface displacement amplitude versus

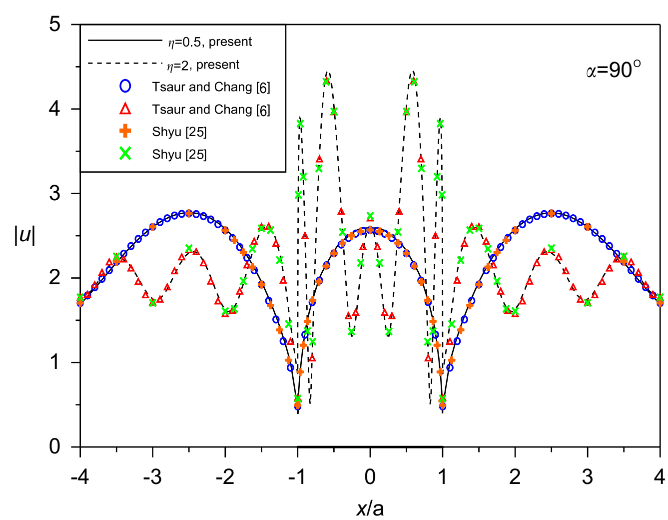

Fig. 5. Displacement amplitudes versus x/a for the incident angle $\alpha=90^{\circ}$.

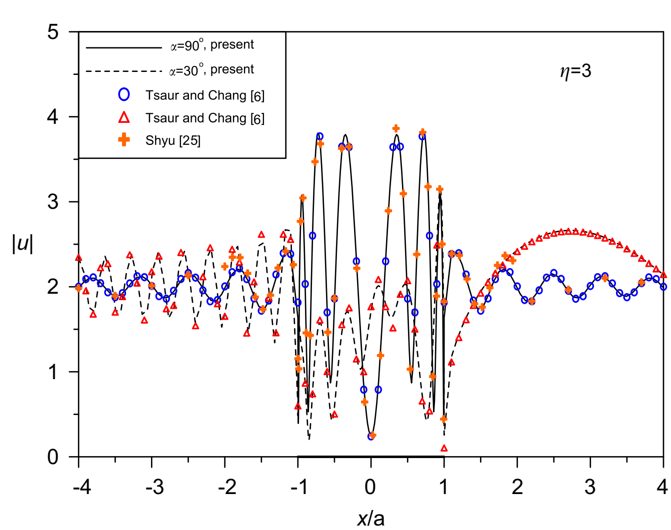

Fig. 6. Displacement amplitudes versus x/a for the dimensionless frequency $\eta=3$.

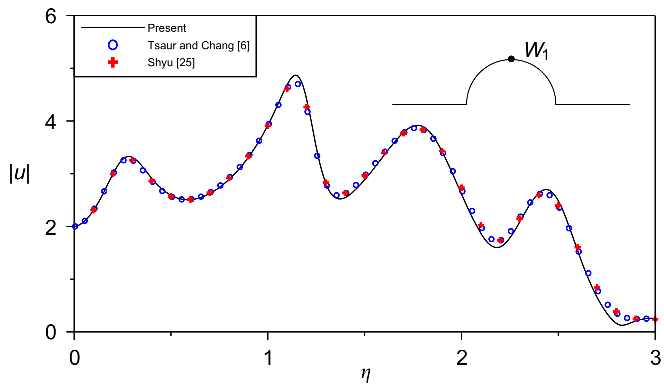

Fig. 7. Surface displacement amplitudes for the point W_1 versus η for the incident angle $\alpha=90^\circ$.

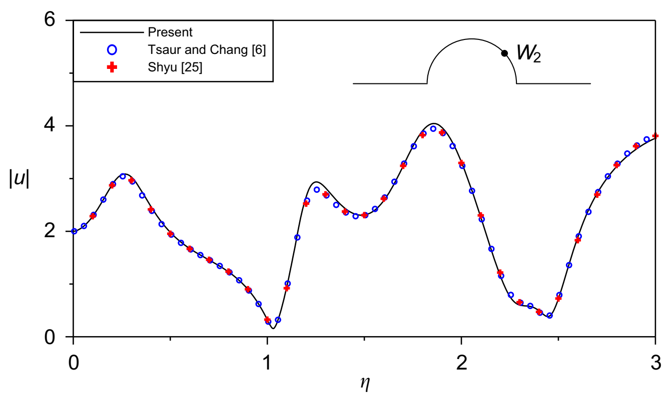

Fig. 8. Surface displacement amplitudes for the point W_2 versus η for the incident angle $\alpha=90^\circ$

x/a for the dimensionless frequencies $\eta=0.5$ and 2 subject to the SH wave for incident angle $\alpha=90^\circ$ and a good agreement is made. Fig. 6 shows the surface displacement amplitude versus x/a for $\eta=3$ and the incident angles of $\alpha=90^\circ$ and $\alpha=30^\circ$. Besides, the surface displacement amplitudes at the specified location of hill border versus η were compared with those of Shyu [25] and Tsaur and Chang [6] as shown in Figs. 7 and 8. It is noted that Tsaur and Chang employed the approach wave function expansion in conjunction with the region matching technique. Shyu's results were obtained using the hybrid method. Acceptable results are obtained.

In Fig. 9, it is interesting to find that high displacement amplitude is observed in a localized area for the case of incident angle of 90° and $\eta=3$. This phenomenon is the so-called the focusing effect as well as in optics and acoustics. A similar phenomenon for a shallow circular hill has been found by Tsaur and Chang [6] in both time and frequency domains.

7. Conclusions

In this paper, the SH-wave problem scattered by a semi-circular hill was revisited. By taking free body, the original problem can be decomposed into two subdomains. For the half-plane with a half circular arc, it is designed to be imbedded in an infinite domain with a full circular boundary. Due to the property of a full circular boundary, we naturally employed the null-field BIEM in conjunction with degenerate kernel and Fourier series. After constructing six constraint equations through two subdomains and four boundary conditions instead of selecting admissible wave function bases, a linear algebraic equation is obtained. Then, unknown Fourier coefficients were determined solving the linear algebraic equation. To test the validity of our formulation, our results were compared well with those of Shyu, and Tsaur and Chang in the literature. Besides, a focusing effect was also observed.

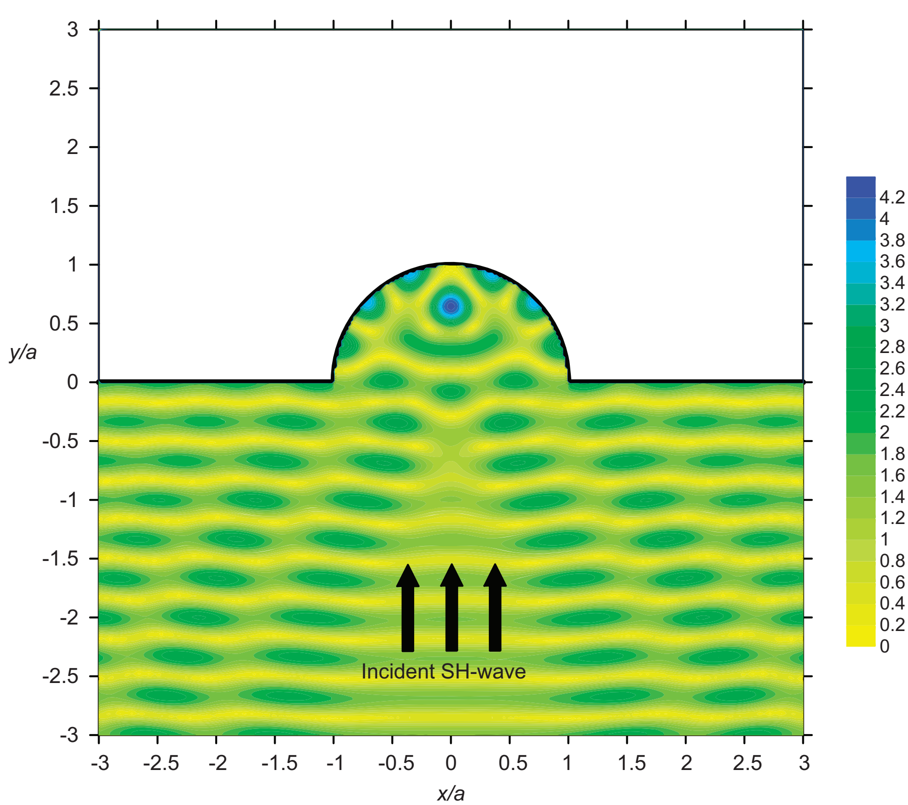

Fig. 9. Contour plot of displacement amplitude for $\eta=3$ and incident angle $\alpha=90^\circ$.

Acknowledgements

Financial support from the National Science Council under Grant no. NSC97-2221-E-019-015-MY3 for the National Taiwan Ocean University is gratefully acknowledged. The authors also thank Drs. Tsaur and Chang for providing the results using the wave function expansion approach and the region matching idea. Besides, Dr. Shyu's results using the hybrid method are also appreciated.

Appendix

Degenerate kernels of $\partial U^E(\mathbf{s},\mathbf{x})/\partial\rho$, $\partial U^E(\mathbf{s},\mathbf{x})/\partial\phi$, $\partial T^E(\mathbf{s},\mathbf{x})/\partial\rho$ and $\partial T^E(\mathbf{s},\mathbf{x})/\partial\phi$ for the polar coordinates are given below:

$$\frac{\partial U(\mathbf{s},\mathbf{x})}{\partial\rho}=\begin{cases}\frac{\partial U^E(\mathbf{s},\mathbf{x})}{\partial\rho}=\lim\limits_{N\to\infty}\frac{-\pi ki}{2}\sum\limits_{m=0}^{N}\varepsilon_m J_m(kR)H'^{(1)}_m(k\rho)\cos(m(\theta-\phi)), & \rho\ge R,\\ \frac{\partial U^I(\mathbf{s},\mathbf{x})}{\partial\rho}=\lim\limits_{N\to\infty}\frac{-\pi ki}{2}\sum\limits_{m=0}^{N}\varepsilon_m J'_m(k\rho)H^{(1)}_m(kR)\cos(m(\theta-\phi)), & \rho<R,\end{cases} \tag{A.1}$$

$$\frac{\partial U(\mathbf{s},\mathbf{x})}{\partial\phi}=\begin{cases}\frac{\partial U^E(\mathbf{s},\mathbf{x})}{\partial\phi}=\lim\limits_{N\to\infty}\frac{-\pi i}{2}\sum\limits_{m=0}^{N}m\varepsilon_m J_m(kR)H^{(1)}_m(k\rho)\sin(m(\theta-\phi)), & \rho\ge R,\\ \frac{\partial U^I(\mathbf{s},\mathbf{x})}{\partial\phi}=\lim\limits_{N\to\infty}\frac{-\pi i}{2}\sum\limits_{m=0}^{N}m\varepsilon_m J_m(k\rho)H^{(1)}_m(kR)\sin(m(\theta-\phi)), & \rho<R,\end{cases} \tag{A.2}$$

$$\frac{\partial T(\mathbf{s},\mathbf{x})}{\partial\rho}=\begin{cases}\frac{\partial T^E(\mathbf{s},\mathbf{x})}{\partial\rho}=\lim\limits_{N\to\infty}\frac{-\pi k^2 i}{2}\sum\limits_{m=0}^{N}\varepsilon_m J'_m(kR)H'^{(1)}_m(k\rho)\cos(m(\theta-\phi)), & \rho>R,\\ \frac{\partial T^I(\mathbf{s},\mathbf{x})}{\partial\rho}=\lim\limits_{N\to\infty}\frac{-\pi k^2 i}{2}\sum\limits_{m=0}^{N}\varepsilon_m J'_m(k\rho)H'^{(1)}_m(kR)\cos(m(\theta-\phi)), & \rho<R,\end{cases} \tag{A.3}$$

$$\frac{\partial T(\mathbf{s},\mathbf{x})}{\partial\phi}=\begin{cases}\frac{\partial T^E(\mathbf{s},\mathbf{x})}{\partial\phi}=\lim\limits_{N\to\infty}\frac{-\pi ki}{2}\sum\limits_{m=0}^{N}m\varepsilon_m J'_m(kR)H^{(1)}_m(k\rho)\sin(m(\theta-\phi)), & \rho>R,\\ \frac{\partial T^I(\mathbf{s},\mathbf{x})}{\partial\phi}=\lim\limits_{N\to\infty}\frac{-\pi ki}{2}\sum\limits_{m=0}^{N}m\varepsilon_m J_m(k\rho)H'^{(1)}_m(kR)\sin(m(\theta-\phi)), & \rho<R.\end{cases} \tag{A.4}$$

References

[1] Chen JT, Chen PY, Chen CT. Surface motion of multiple alluvial valleys for incident plane SH-waves by using a semi-analytical approach. Soil Dyn Earthq Eng 2008;28:58–72.

[2] Trifunac MD. Surface motion of a semi-cylindrical alluvial valley for incident plane SH waves. Bull Seism Soc Am 1971;61(6):1755–70.

[3] Trifunac MD. Scattering of plane SH waves by a semi-cylindrical canyon. Earthq Eng Struct Dyn 1973;1:267–81.

[4] Yuan X, Liao ZP. Scattering of plane SH waves by a cylindrical canyon of circular-arc cross-section. Soil Dyn Earthq Eng 1994;13:407–12.

[5] Vogt RF, Wolf JP, Bachmann H. Wave scattering by a canyon of arbitrary shape in a layered half-space. Earthq Eng Struct Dyn 1988;16:803–12.

[6] Tsaur DH, Chang KH. Scattering and focusing of SH waves by a convex circular-arc topography. Geophys J Int 2009;177:222–34.

[7] Yuan X, Men FL. Scattering of plane SH waves by a semi-cylindrical hill. Earthq Eng Struct Dyn 1992;21:1091–8.

[8] Yuan X, Liao ZP. Surface motion of a cylindrical hill of circular-arc cross-section for incident plane SH waves. Soil Dyn Earthq Eng 1996;15:189–99.

[9] Mei CC. Boundary layer and finite element techniques applied to wave problem. In: Varadan VV, Vardan VK, editors. Acoustic, Electromagnetic and Elastic Wave Scattering-Focus on the T-Matrix Approach. New York: Pergamon; 1980.

[10] Komatitsch D, Liu Q, Tromp J, Süss P, Stidham C, Shaw JH. Simulations of ground motion in the Los Angeles basin based upon the spectral-element method. Bull Seism Soc Am 2004;94:187–206.

[11] Kawakami H, Mogi H. Analysis of scattered waves on ground with irregular topography using the direct boundary element and Neumann series expansion. Bull Seism Soc Am 2007;97(4):1144–57.

[12] Álvarez-Rubio S, Sánchez-Sesma FJ, Benito JJ, Alarcón E. The direct boundary element method: 2D site effects assessment on laterally varying layered media (methodology). Soil Dyn Earthq Eng 2004;24:167–80.

[13] Sánchez-Sesma FJ, Vai R, Dretta E. The variational indirect boundary element method: a strategy toward the solution of very large problems of site response. J Comput Acoust 2001;9(2):531–41.

[14] Kawase H. Time-domain response of a semi-circular canyon for incident SV, P and Rayleigh waves calculated by the discrete wavenumber boundary element method. Bull Seism Soc Am 1988;78(4):1415–37.

[15] Lee VW, Luo H, Liang JW. Antiplane (SH) waves diffraction by a semicircular cylindrical hill revisited: an improved analytical wave series solution. ASCE J Eng Mech 2006;132(2):1106–14.

[16] Sánchez-Sesma FJ, Herrera I, Avilés J. A boundary method for elastic wave diffraction: application to scattering of SH waves by surface irregularities. Bull Seism Soc Am 1982;72(2):473–90.

[17] Chen JT, Wu AC. Null-field approach for the multi-inclusion problem under antiplane shears. J Appl Mech—T ASME 2007;74:469–87.

[18] Chen JT, Chen CT, Chen PY, Chen IL. A semi-analytical approach for radiation and scattering problems with circular boundaries. Comput Meth Appl Mech Eng 2007;196:2751–64.

[19] Chen JT, Hsiao CC, Leu SY. A new method for Stokes problems with circular boundaries using degenerate kernel and Fourier series. Int J Numer Meth Eng 2008;74:1955–87.

[20] Lee WM, Chen JT. Scattering of flexural wave in a thin plate with multiple circular inclusions by using the null-field integral equation approach. J Sound Vibr 2010;329:1042–61.

[21] Fu LY. Rough surface scattering: comparison of various approximation theories for 2D SH waves. Bull Seism Soc Am 2005;95:646–63.

[22] Kamalian M, Jafari MK, Sohrabi-Bidar A, Razmkhah A. Seismic response of 2-D semi-sine shaped hills to vertically propagating incident waves: amplification patterns and engineering applications. Earthq Spect 2008;24(2): 405–30.

[23] Lee JJ. Wave-induced oscillation in harbors of arbitrary geometry. J Fluid Mech 1971;45:375–94.

[24] Wood Jr. WD, Wood AW. Development and numerical solution of integral equations for electromagnetic scattering from a trough in ground plane. IEEE Trans Antennas Propag 1999;47(8):1318–22.

[25] Shyu WS. Private communication; 2010.